LAWRENCE
LIVERMORE
NATIONAL
LABORATORY

LLNL-PROC-678463

Light Scattering from Laser-Induced Shallow Pits on Silica Exit Surfaces

E. Feigenbaum, R. N. Raman, N. Nielsen, M. J. Matthews

October 20, 2015

XLVII Annual Symposium on Optical Materials for High-Power Lasers
Boulder, CO, United States
September 27, 2015 through September 30, 2015

Disclaimer

Light Scattering from Laser-Induced Shallow Pits on Silica Exit Surfaces

E. Feigenbaum*[a], R. N. Raman [a], N. Nielsen [a], and M. J. Matthews [a]
National Ignition Facility and Photon Science, Lawrence Livermore National Laboratory,
7000 East Ave., Livermore, California 94550, USA

ABSTRACT

We study the formation of laser-induced shallow pits (LSPs) on silica output surfaces and relate these features to optical performance as a function of incident laser fluence. Typical characteristics of the LSPs morphology are presented. Closed-form expressions for the scattered power and far-field angular distribution are derived and validated using numerical calculations of both Fourier optics and FDTD solutions to Maxwell's equations. The model predictions agree well with the measurements for precise profile micro-machined shallow pits on glass, and for pitting caused by laser cleaning of bound metal micro-particles at different fluences.

Keywords: Laser damage, Scattering.

1. INTRODUCTION

A substantial effort has been spent in the last decade on mitigating damage sites initiation in high power lasers optics and on the suppression of their shot-to-shot growth [1-5]. These growing damage sites can be characterized by their complex fracture-dominated morphologies and while only a few tens of microns in depth they have the potential to limit optics lifetime. On the other hand, much shallower laser-induced pits (i.e., sub-micron deep) that are free of fracture and appear on optics in greater densities are the subject of fewer studies since they do not change morphology under subsequent laser pulses (i.e. no growth), and do not lead to direct optics lifetime limitations [6-9]. The evaluation of the resulting light scattering is important, since it might lead to a reduction of power on target as well as unintended irradiation of other optics [6].

We will detail the typical characteristics of LSPs and present relatively simple analytical relations between the observed morphology of the LSPs and the power scattering at the far-field [6]. We will bring validation to this model for precisely shaped micro-machined sample, using a power scattering measurement, and further study the morphology-scattering relations for pitting caused by laser cleaning of bound metal micro-particles at different fluences [10].We note that these expressions could also be utilized for a carefully designed beam shaping optic based on LSP clusters [10].

2. THE PROPERTIES OF LSPS

LSPs are a result of laser interaction with metal micro-particulates on glass exit surface. The incident laser beam deposits heat into the skin layer of the metal particle, which in turn emits a plasma emission towards the substrate surface, which propels the particle away from the substrate, and also etches away a LSP on it (a broader discussion in the underlying physics of the LSPs formation is outside the scope of this paper, and will be discussed in [11]). This LSP formation process is illustrated in Figure 1 (a) and (b). The density of LSPs found on test samples (of the same type observed also on the NIF final optics glass) can be as high as 1500 per mm^2. This relatively high density motivates the evaluation of the resulting power scattering, as illustrated in Figure 1(c), where the LSP ensemble results in a scatter halo around the far-field designed spot.

Next we will detail some of the observed LSPs typical characteristics. The LSPs are axisymmetric Gaussian-like shallow pits, with typical width ranging from few microns to few tens of microns, and few hundreds nanometers deep. The depth of the LSPs and their width are correlated, and while the small LSPs have Gaussian-like profile, the larger ones show formation of 'shoulders' (as illustrated in the formed LSP shape in Figure 1(b)). As the incident fluence increase, their depth increases too, which will be described in more details hereafter in section 6.

*Corresponding author: eyalf@llnl.gov

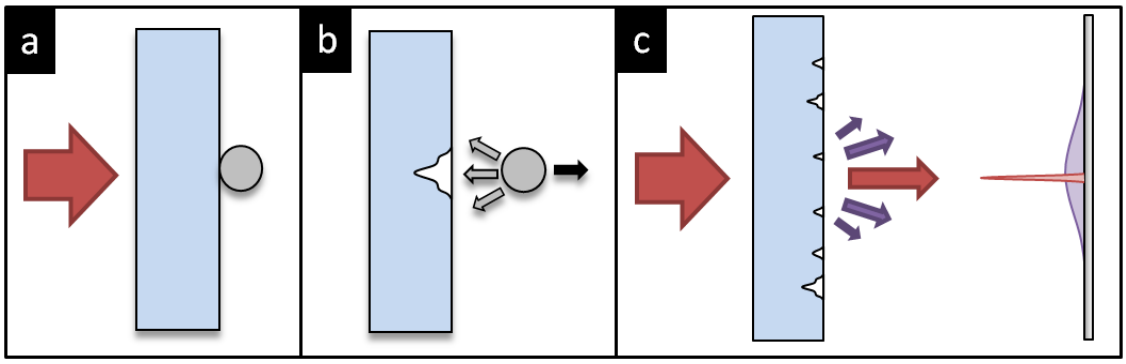

Figure 1. Schematic illustration of the studied problem - creation of laser-induced shallow pits (LSPs) and light scattering from it: (a) high power laser incident on glass, with metal particles on its exit surface, (b) the energy deposited in the metal generates plasma that propels the particulate and etches the glass surface, (c) when subsequent laser shots illuminate the glass, the ensemble of the previously created LSPs scatter part of the incident beam, resulting in a halo around the far-field spot.

3. MODEL FOR THE SCATTERED POWER MODEL FROM LSPS [6]

Without a more informed method of relating the light scattering to the LSPs morphology, one possible approach is to assume that all light that incident on their aperture will not reach the far-field. This assumption will typically over-estimate their true power scatter contribution. Nevertheless, the specific and smoothly varying morphology of the LSP justifies a more informed analysis.

As a first step we have confirmed that the far-field scatter is well represented using Fourier optics (i.e., that the paraxial approximation is adequate, and that near field scattering waves effects are negligible) by comparison of the Fourier beam propagation method to Finite-Difference Time-Domain (FDTD) numerical calculations of Maxwell's equations (Lumerical Solutions Inc., Vancouver, Canada). The illumination light used here is in the ultra-violet with a free-space wavelength of 351 nm (i.e., as in the final optics of the NIF). The electric field at 5 μm of the surface based on 1D-FDTD calculation was compared to the Fresnel paraxial calculation. When the fields from both calculations were propagated (using FFT based far-field propagator) the difference in magnitude at far-field was very slight, few percent at most. Furthermore, for all the cases examined, the calculated scattered power using the paraxial approximation set a tight upper bound to the FDTD results, likely resulting from the large-k vector scattering included only in the latter.

Next, we derive an analytic expression for the power scattering from a Gaussian shaped pit in glass based on Fourier optics. We represent the phase distribution as a Taylor expansion of amplitude Gaussians. This is motivated by the fact that the propagation of an amplitude-shaped Gaussian is analytically resolved (i.e, Gaussian transforms into a Gaussian at far-field, with known analytic parameters), and by the fact that the transformation to far-field is linear. The incident plane wave electric field right after passing through the Gaussian phase object (with maximal depth of h and standard deviation σ) and the equivalent expansion is:

$$E(r) = A_{NF} e^{i\phi} = A_{NF} \left\{ 1 + \sum_{m=1}^{\infty} \frac{(i)^m}{m!} \phi^m \right\} \tag{1}$$

The contribution of the zeroth order term, associated with the non-scattered plane wave, evolves into diffraction limited spot at the far-field, and is not part of the scattered light discussed hereafter. The electric field of the scattered light at far-field is:

$$E_{FF} = A_{NF} \sum_{m=1}^{\infty} \frac{i^m \cdot OPD^m \cdot \sigma^2}{\gamma \cdot m \cdot m!} \cdot \exp\left(-\frac{\sigma^2}{\gamma^2 \cdot m} \cdot r^2 \right) \tag{2}$$

where, A_{NF} is the near field amplitude of the incident wave, OPD is the maximal optical path difference: $OPD = -2\pi \cdot \Delta n \cdot h / \lambda$, λ is the free-space wavelength, Δn is the absolute value of the refractive index difference

between the substrate and surrounding media (air), $\gamma = \lambda z / \pi$, z is the propagation distance off the exit surface, and r is the radial transversal coordinate. We find that finite effective series is a sufficient far-field representation for the typical LSP shapes found on exit surface of contamination-driven ablation, by comparing of the expression in Eq. (2) with the numerical far-field solution based on 2D-FFT propagator. For example, in Fig. 2(a) the convergence of Eq. (2) expression to the solution is illustrated as the series length is being varied for a 250 nm depth and σ = 2 μm Gaussian LSP, showing an effective required series length of m~7 terms for this case.

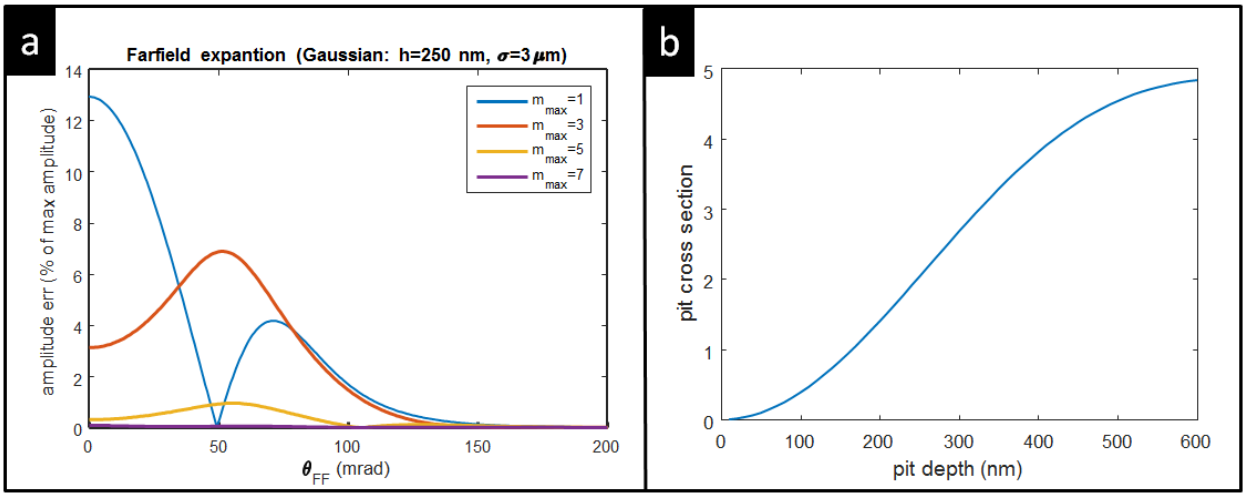

Figure 2. Scattering of single Gaussian shaped LSP: (a) Convergence of the far-field expansion (Eq. (2)) to the solution with increasing series length. The far-field irradiance error is presented (absolute value) as a percent of the maximum amplitude. (b) Scattering cross-section (ξ) as function of LSP depth (m_{max}=50).

The first term in the far-field series representation (m=1) captures well the lower moments of the field distribution, and allows for a simple evaluator of the scattered light cone angle:

$$\theta_{FF} \sim \frac{\lambda}{\pi \cdot \sigma} \tag{3}$$

This angle increases with decreasing LSP width, but is independent of its depth. The maximal intensity, based on the first term, is proportional to $I_{FF} \propto h^2 \cdot \sigma^4$, which can be correlated to the Rayleigh-Gans scattering intensity which is also proportional to the particle volume squared [12]. This observation highlights that the widest and deepest LSPs in the ensemble are more likely to dominate the total far-field intensity distribution.

Based on the spatial integration of the intensity of the field described in Eq. (2) and some algebra, the expression for the scattered power is:

$$P^{scat} = \left(\eta \left|A_{NF}\right|^2 \cdot \pi\sigma^2\right)\left(\sum_{m=1}^{\infty}\sum_{l=1}^{\infty} \frac{i^m \cdot (-i)^l \cdot OPD^{m+l}}{(m+l) \cdot m! \cdot l!}\right) \tag{4}$$

where η is the free-space wave impedance. The resulting scattered power expression could be interpreted as the incident power on a circular area with a 1σ radius, i.e., $\pi\sigma^2$, (first RHS in Eq. (4)) times the cross-section of the LSP (ξ) determined by its OPD (second RHS term). The expression in Eq. (4) is validated and found to be in excellent agreement with the numerical FFT-propagator results. Since the area that a LSP with a Gaussian phase profile covers is unbounded, the unit-less term ξ could exceed a value of one, as seen in Fig. 3(b) to be the case for LSPs deeper than about 160 nm. Using a polynomial fit to Eq. (4) in the 0-250 nm deep range, we find that for LSP depths substantially smaller than 1 μm, the scattered power is scaling proportionally to h^2. Since the height of the LSP is proportional to their width (e.g., see Fig. 5 (b)), for a LSP with one order of magnitude smaller width the scattered power is expected to be several orders of magnitude smaller.

The intensity of LSPs ensemble is obtained as the incoherent addition of the individual LSPs intensities, justified by the large and aperiodic distances between the LSPs with respect to their widths. For LSPs with non-Gaussian profiles close agreement to model is obtained using an effective σ (σ_{eff}) of a Gaussian shaped pit having the same volume as the examined LSP (where volume is defined as $2\pi\int d(r)\cdot rdr$, d(r) being the depth profile). We have examined and validated this model for LSPs with "shoulders" and also for a different identified shaped surface pit, typically found on laser optics which undergo chemical etching to enhance damage performance [2], having a shallow parabolic shaped profile.

4. POWER SCATTER MEASUREMENT [10]

The scattered light around the optical axis from a pitted glass sample is characterized at the ultraviolet frequency range using the experimental setup illustrated in Fig. 3. The laser beam emitted from a ~5 mW 351 nm quasi-CW laser (CrystaLaser QUV-351-200) is spatially filtered and expanded using a typical pinhole arrangement to about a 2 cm diameter Gaussian beam spot on the sample. Using illumination fluences much lower than the typical ones for high-power laser systems is justified by the LSPs being sub-micron in depth and on the exit surface of the glass, which is expected to result in negligible nonlinear effects in the light propagation. After the light passes through the sample it propagates to the far-field where it illuminates a Lambertian diffuse screen (Avian B250 - Barium Sulfate based coating). The scattered power is typically a fraction of a percent of the incident beam and therefore the diffuse surface has a center perforation that transmits the un-scattered beam to reduce backscattering. An ultraviolet sensitive CCD camera with programmable high speed electronic shutter (Spiricon SP620U) is used to image the far-field screen.

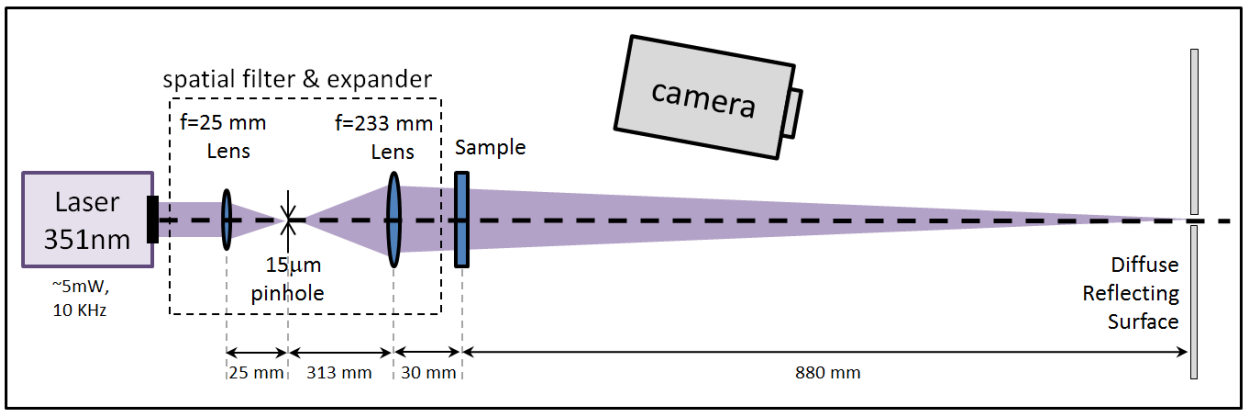

Figure 3. Scattered power and irradiation experimental setup layout: expanded and filtered ultraviolet laser beam is passed through the sample, and hit a diffuse screen at far-field, which is imaged by programmable high speed electronic shutter CCD camera.

Post-processing of the images is used in order to subtract the background and average out the noise. The background is measured by taking the same measurement without the sample and is then subtracted from the measurement with the sample. The main two noticeable background artifacts are bias base level and scattering around the perforation at the screen center. For both cases with the sample (i.e., signal) and without it (i.e., background), 16 successive camera image frames have been averaged to reduce the noise level.

In order to normalize the scattered power by the beam total power, an additional measurement is taken imaging the entire beam reflecting off the surface. This measurement is performed without the sample and by shifting the diffuse screen such that the beam does not go through the perforation. Since the signal for this measurement is about 4 orders of magnitude higher than that of the scattered power the camera integration time is much shorter. For this whole beam measurement the noise is also being averaged out using 16 successive frames and the bias background level to be offset is calculated from off-axis regions. The scattered irradiation and the integrated scattered power presented hereafter are reported as a fraction of the incident total power.

5. COMPARISON OF MODEL PREDICTIONS AND MEASURED SCATTERING FROM MICRO-MACHINED PITS [10]

In order to validate the model predictions, we have fabricated a sample with a quasi-random ensemble of micro-machined (M-M) shallow pits with similar dimensions using laser ablation. The pit profiles being similar simplify the analysis and validation. The sample morphology is measured using 3D laser scanning confocal microscopy (VK-X110, Keyence Corporation, Elmwood Park, NJ). The surface morphology of one of the M-M pits is illustrated in Fig. 4 (a). Since the M-M pits are not Gaussian their σ_{eff} was evaluated based on their calculated volume to be 11.3 ± 1.3 μm.

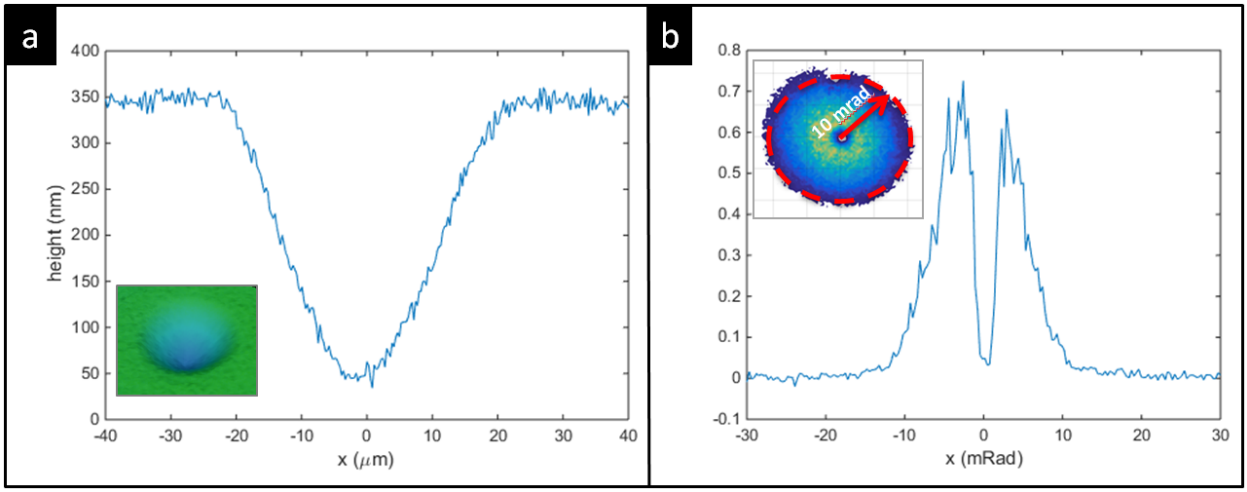

Figure 4. Scattering from micro-machined (M-M) pits on silica substrate: (a) height profile of a typical M-M pit, with a 3D rendering of topology as inset, (b) Profile of the measured scattered irradiation, with 2D distribution as an inset (values in A.U.).

The measured scattering angle was found to be in excellent agreement with the predicted by the model. Based on the mean σ_{eff} observed for the sample morphology and Eq. (3) the predicted scatter angle is: $\theta_{FF} \sim 10.02 \pm 1.15\ mrad$. The measured scattered irradiance is depicted in Fig. 4 (b), obtained based on the methodology described in section 4. The θ_{FF} refers to the angle at which the field intensity decays to $1/e^2$ of its peak value, measured to be θ_{FF} ~10 mrad (see Fig. 4(b)), which matches the predicted value.

The scattered power fraction of the beam (with respect to the total power incident on the surface) based on Eq. (4) is:

$$\frac{P^{scat}}{P} = \frac{N\pi\sigma^2}{S}\xi \tag{5}$$

where N is the number of M-M pits in the area over which the calculation is done, S. For the sample under evaluation, the average density of M-M pits is about 10 per mm^2 and the measured depth is 300 nm giving a cross-section of 2.7. Therefore the predicted scattered power is 1% of the total power. The measured scattered power is 0.75±0.05% of the total beam power, which is tightly bounded by the predicted value. The model prediction is expected to be slightly higher than the measurement, due to some small fraction of high-angles scattering that does not reach the far-field [6].

6. SCATTERING FROM LASER-INDUCED SHALLOW PITS DERIVED FROM SURFACE BOUND PARTICLES [10]

After validating the scattered power measurement setup with the model, we now turn to study the scattering when the beam is incident on pitted exit surface of silica glass samples – representative of metal particle laser ablation. The samples were prepared by sprinkling 20 μm diameter spherical aluminum particles on the exit surface of 4 silica slabs (this procedure is further detailed in [9]), after surface cleaning and HF-etching (see details in [3]). Each sample has been exposed to a large aperture (~ 3 cm diameter) 5 ns pulsed (flat-in-time) laser in the ultraviolet (λ=351 nm) at a different fluence [14]: 2 J/cm^2, 5 J/cm^2, 8 J/cm^2, and 11 J/cm^2. The morphology of the surface has been characterized using

confocal laser scanning microscope. A scan area of 2.5 mm x 2.5 mm has been stitched together from multiple high resolution sub scans at lateral resolution of 0.5 μm per pixel and depth resolution of 0.1 nm per vertical pixel, and linear tilt has been corrected. The height maps of representative segments at the four samples are presented at Fig. 5 (a), where black regions indicate depressions in the surface. This collected data shows increased amount of pitting for samples with higher laser exposure, and also shows that at the low fluence sample a larger number of bound particles have remained.

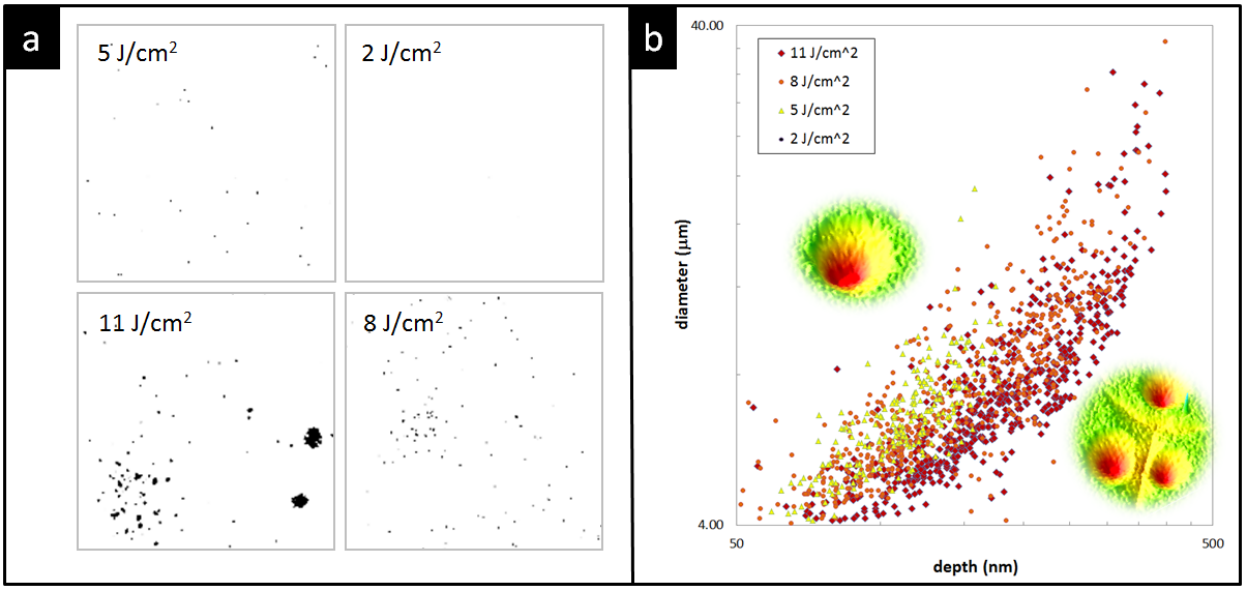

Figure 5. The morphology of the silica sample exit surface pitting induced by laser cleaning of metal micro-particle: (a) height maps of the representative segments at the four samples (1.25 mm x 1.25 mm) induced by different fluences indicated on the image (black indicates depression). (b) Pit dimension analysis of the detected pits population for the 4 samples, along with 3D height rendering of LSP, and LSPs bunch.

To better characterize the dimensions of the LSPs on the four samples we have processed the image resulting in a list of the width and depth of the measured surface depressions. Image processing was conducted to threshold the image (ImageJ, National institutes of Health, USA) to find the depressions in the sample and particle analysis to characterize the dimensions of the detected segments. To enhance the statistics we have included two 2.5 mm x 2.5 mm scanned segments per sample. The results are depicted in Fig. 5 (b) on a log-log scale. Only on the 11 J/cm^2 sample growing damage sites (classified as a type III in [13]) have been detected. These two detected laser damage sites clearly appear in Fig. 5 (a) as the two large irregularly shaped black regions. The other type of laser induced features found much more abundantly on the surface are the LSPs, are illustrated as a 3D rendering in Fig. 5 (b). These axisymmetric, Gaussian-like profiles are the main focus of this paper, and appear as single LSPs in these four samples, more often in bunches of LSPs spaced by linear-like groove in the high fluence shot.

Based on the morphology characteristics described in Fig. 5, the power scatter predicted by the model fits well the observations from the scatter measurement. The scatter measurements for the four samples are shown in Fig. 6. It is immediately clear from the scattered power (at the subplot titles) and the irradiance that the scatter increase as the sample was exposed to higher fluence, as expected due to deeper and more abundant pitting. On the 2 J/cm^2 sample only a small amount of existing particles where detected, and the scattered power level detected is very small having almost flat irradiance – at the measurement noise level. As the laser fluence is increased, the population of detected LSPs has higher diameter and depth – expected to result in a higher scattered power from the LSPs population. The diameter of the dominant LSPs for the 11 J/cm^2 sample is about 30 μm, which translates based on Eq. (3) to an expected scatter angle of about 20 mrad – which fits the measurement in Fig. 6 (d) (see the dashed line indicated by (B)). For the 8 J/cm^2 case, the LSPs diameter is similar but the depth is slightly smaller, the resulting scatter is lower in magnitude but has similar scatter angle. For the 5 J/cm^2 sample the dominant LSPs diameter is about 10 μm and also smaller in depth and number of counts, and therefore expected to have smaller magnitude of scatter and a broader angle. The magnitude reduction is clearly observed in the measurement. However, even though a small broadening could be observed in the scatter irradiation curve, it is hard to examine the broadening since the measured signal is reaching at these scatter angles close

to the measurement noise level. Finally, the two detected laser damage sites for the 11 J/cm^2 sample have very large volumes and therefore are expected to result in a large scatter contribution for this sample. Since their diameter is about 100 μm, they are expected to yield an additional feature of few mrad scatter angle as clearly seen in Fig. 6 (d) (see the dashed line indicated by (A)). The clear correlation made by the model between the scattered power measurements to the sample morphology, indicates also that analysis of the scatter irradiance based on the model could serve as a method indicating the presence of scattering features on samples.

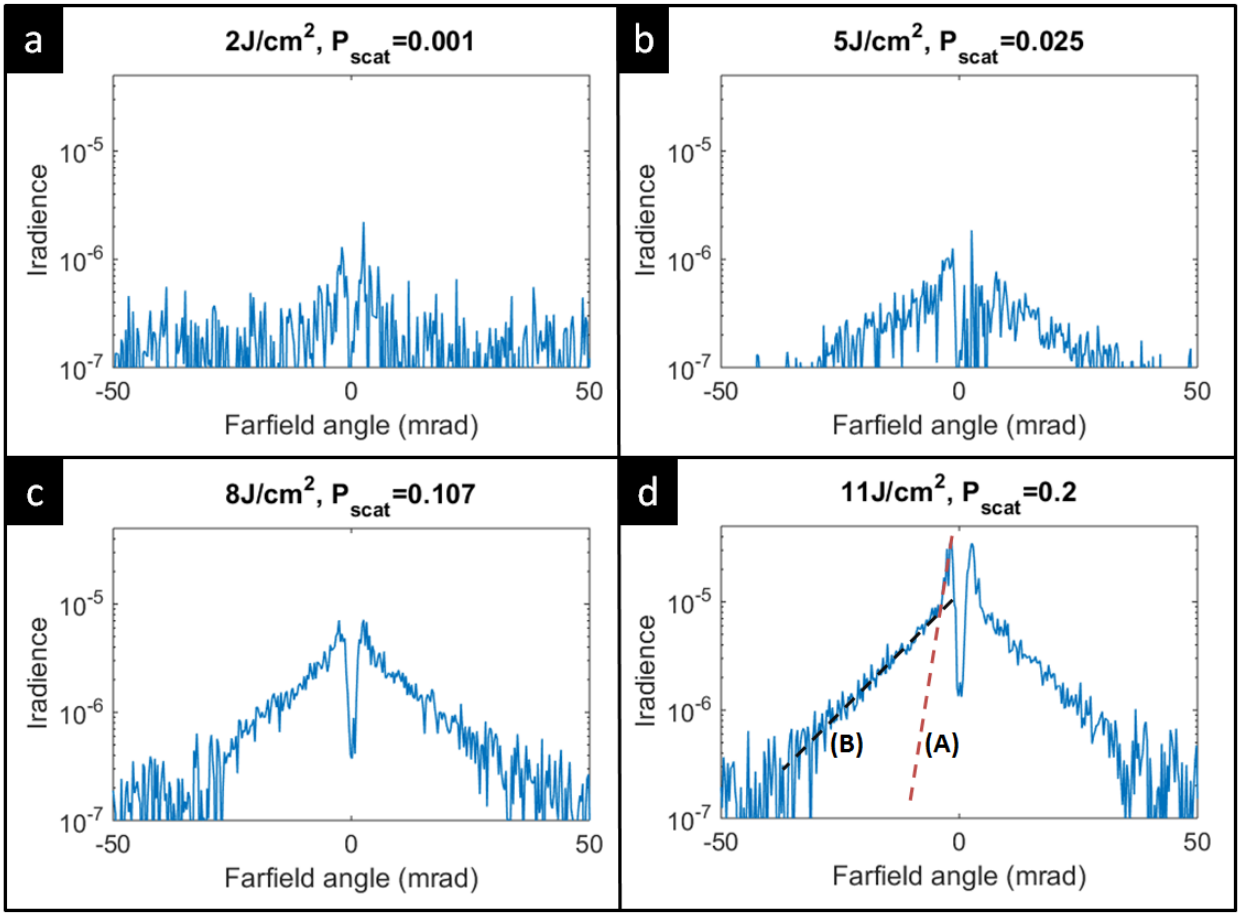

Figure 6. Scatter irradiance profile of the four laser induced damage samples (presented in Figure 5). The scattered power as a fraction of the incident beam power is given at the title in units of % (±0.015%).

7. CONCLUSIONS

In summary, we have developed here simple relations between the scattered power and irradiance and the morphology of the Gaussian shaped shallow pits scattering objects, and extended the model to other shapes of shallow pits. The analysis was validated and exercised in the framework of the laser-induced shallow pits (LSPs) observed in the NIF final optics characterized by a large number of sub-micron deep and few microns wide LSPs in fused silica, which scatters an ultra-violet laser beam. The model predictions were found to be in excellent agreement to the measurement for the precise profile micro-machined shallow pits. Furthermore, the resulting scattering from pitting caused by laser cleaning of bound metal micro-particles at different fluences, show good agreement with the model predictions. The model allows inference from the observed features in the irradiance measurement about the morphology and the types of scattering object present on the sample.

ACKNOWLEDGEMENTS

We would like to acknowledge Gabe Guss for preparing the designed sample described in Fig. 4, and to acknowledge the optical sciences laboratory (OSL) staff for preparing the laser cleaning samples described in Fig. 5. This work was performed under the auspices of the U.S. Department of Energy by Lawrence Livermore National Laboratory under contract DE-AC52-07NA27344. We would like to acknowledge the funding from Laboratory Directed Research and Development grant 14-ERD-098. [LLNL-PROC-678463]

REFERENCES

[1] S. G. Demos, M. Staggs, K. Minoshima, J. Fujimoto, "Characterization of laser induced damage sites in optical components," Opt. Express 10, 1444-1450 (2002)

[2] B. Bertussi, P. Cormont, S. Palmier, P. Legros, J. Rullier, "Initiation of laser-induced damage sites in fused silica optical components," Opt. Express 17, 11469-11479 (2009).

[3] T. I. Suratwala, P. E. Miller, J. D. Bude, W. A. Steele, N. Shen, M. V. Monticelli, M. D. Feit, T. A. Laurence, M. A. Norton, C. W. Carr, L. L. Wong "HF-based etching processes for improving laser damage resistance of fused Silica optical surfaces," J. Am. Ceram. Soc. 94, 416–428 (2011).

[4] I. L. Bass, G. M. Guss, M. J. Nostrand, P. L. Wegner, "An improved method of mitigating laser-induced surface damage growth in fused Silica using a rastered, pulsed CO2 laser", Proc. SPIE 7842, Laser-Induced Damage in Optical Materials: 2010, 784220

[5] M.J. Matthews, S.T. Yang, N. Shen, S. Elhadj, R.N. Raman, G. Guss, I.L. Bass, M.C. Nostrand, P.J. Wegner, "Micro-Shaping, Polishing, and Damage Repair of Fused Silica Surfaces Using Focused Infrared Laser Beams," Advanced Engineering Materials 17, 247-252 (2015)

[6] E. Feigenbaum, S. Elhadj, M.J. Matthews, "Light scattering from laser induced pit ensembles on high power laser optics," Opt. Express 23, 10589-10597 (2015).

[7] S. Palmier, I. Tovena, L. Lamaignère, J. L. Rullier, J. Capoulade, B. Bertussi, J. Y. Natoli, L. Servant, "Study of laser interaction with aluminum contaminant on fused silica," Laser-Induced Damage in Optical Materials 2005, Proc. of SPIE Vol. 5991 59910R

[8] B.S. Luk`yanchuck, Laser Cleaning, Chapter 3, (World Scientific, 2002)

[9] M.J. Matthews, N. Shen, J. Honig, J.D. Bude, A.M. Rubenchik, "Phase modulation and morphological evolution associated with surface-bound particle ablation," J. Opt. Soc. Am. B 30, 3233 (2013)

[10] E. Feigenbaum, N. Nielsen, M.J. Matthews, "Measurement of optical scattered power from laser-induced shallow pits on silica," Appl. Opt. 54, 8554-8560 (2015).

[11] N. Shen, S. G. Demos, R. A. Negres, A. M. Rubenchik, C. D. Harris, M.J. Matthews, "Energetic laser cleaning of metallic particles and surface damage on silica optics: Investigation of the underlying governing mechanisms," SPIE Laser damage 2015

[12] H. C. van de Hulst, Light Scattering by Small Particles (Dover, NY, 1981)

[13] R. A. Negres, D. A. Cross, Z. M. Liao, M. J. Matthews, C. W. Carr, "Growth model for laser-induced damage on the exit surface of fused silica under UV, ns laser irradiation," Opt Express 22, 201848 (2014)